

One-Pot Synthesis of Framework Porphyrin Materials and Their Applications in Bifunctional Oxygen Electrocatalysis

Bo-Quan Li, Shu-Yuan Zhang, Xiang Chen, Chen-Yu Chen, Zi-Jing Xia, and Qiang Zhang*

Organic framework materials constructed by covalently linking organic building blocks into framework structures are highly regarded as paragons to precisely control the material structure at the atomic level. Herein, a direct synthesis methodology is proposed as a guidance for the bulk synthesis of organic framework materials. Framework porphyrin (POF) materials are one-pot synthesized to demonstrate the advances of the direct synthesis methodology. The as-synthesized POF materials are intrinsically 2D and exhibit impressive versatility in composition, structure, morphology, and function, delivering a free-standing POF film, hybrids of POF and nanocarbon, and cobalt-coordinated POF. When applied as electrocatalysts for oxygen reduction reaction and oxygen evolution reaction, the cobalt-coordinated POF exhibits excellent bifunctional electrocatalytic performances comparable with noble-metal-based electrocatalysts. The direct synthesis methodology and resultant POF materials demonstrate the ability of controlling materials at the atomic level for energy electrocatalysis.

architectures.^[4] Since then, organic framework materials with various structures have been well designed, synthesized,^[5] and applied in catalysis,^[6] energy conversion,^[7] gas separation,^[8] etc. For instance, Ding et al. reported a Pd-modified covalent organic framework as an efficient catalyst for Suzuki–Miyaura coupling reaction.^[9] Covalent triazine frameworks were found to perform promising photocatalytic performance for hydrogen evolution.^[10] Porous aromatic framework demonstrated an ultrahigh specific surface area (SSA) highly desirable for hydrogen and carbon dioxide storage.^[11] Organic framework materials serve well as advanced materials in various emerging fields.

Although the prospects for organic framework materials are quite promising, their synthesis is complicated, which severely limits their practical applications.

Substrates for organic framework materials are usually high cost and difficult to obtain because highly symmetrical functional groups are required as knots for linkage. In addition, the procedure of synthesis and purification that commonly involves freeze-pump-thaw cycling,^[12] Soxhlet extraction,^[13] or column chromatography,^[7b] is usually strict and demanding. Such complex operations induce grand challenges in repeatability and expanded large-scale production. Besides, the output of organic framework materials is quite low, affording products at milligram level in many cases.^[6b,14] The synthetic issues seriously hold back full demonstration of organic framework materials with unique properties and broad applications.

In order to overcome the above challenges in material synthesis, we proposed a direct synthesis methodology aiming as a guidance for bulk synthesis of organic framework materials. The feedstocks employed are expected to be simple, low cost, and available at large scales. High quality and output of efficient material processing are strongly demanded. To prove this concept, one-pot synthesis strategy that is simple and effective for high yield synthesis is selected in this contribution.^[15]


Framework porphyrin (POF) materials are one-pot synthesized as a demonstration of the direct synthesis methodology. Porphyrin is selected as the structural unit because of its diversity in composition, coordination, and function.^[16] However, porphyrin-based building blocks are dominantly complicated in structure and high cost. The construction and connection of porphyrin building blocks are generally separated, leading to a tedious procedure and low yield.^[17] By retrospectively the original method for porphyrin synthesis demonstrated in Figure S1

1. Introduction

The discovery and application of new materials impulse the progress of human civilization.^[1] Controllable synthesis of materials at the atomic level has always been the “holy grail” in regard to both science and art. Organic framework materials are constructed by linking small organic molecules with multifunctional groups into extended framework structures through covalent bonds, which possess intrinsic directivity and saturability. By applying predesigned organic functional groups, the interactions between each building block are highly specific. Therefore, the structure of organic framework materials can be precisely controlled under reticular chemistry,^[2] making them as an emerging family of advanced materials strongly considered worldwide.^[3]

One typical sample of organic framework materials was reported by Yaghi and co-workers in 2005. Covalent organic frameworks demonstrate unique crystal structures and porous

B.-Q. Li, S.-Y. Zhang, X. Chen, C.-Y. Chen, Z.-J. Xia, Prof. Q. Zhang
Beijing Key Laboratory of Green Chemical Reaction Engineering
and Technology
Department of Chemical Engineering
Tsinghua University
Beijing 100084, China
E-mail: zhang-qiang@mails.tsinghua.edu.cn

 The ORCID identification number(s) for the author(s) of this article can be found under <https://doi.org/10.1002/adfm.201901301>.

DOI: 10.1002/adfm.201901301

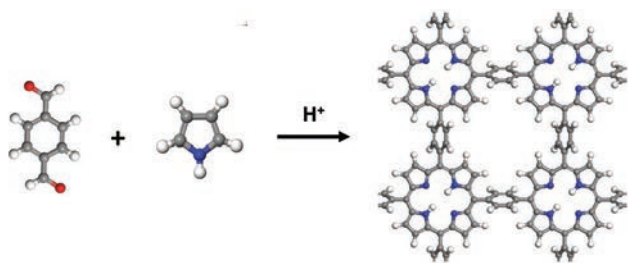


Figure 1. Schematic of the one-pot synthesis of POF. BDA and pyrrole with multifunctional groups go through a dehydration polymerization reaction to construct the 2D structure of POF. The hydrogen, carbon, nitrogen, and oxygen atoms are marked with white, gray, blue, and red, respectively.

(Supporting Information),^[18] we ingeniously proposed the routine for POF fabrication using benzene-1,4-dialdehyde (BDA) instead of benzaldehyde.

As elucidated in **Figure 1**, the π electrons of pyrrole attack the carbonyl groups of BDA activated by protons to afford tetragonal symmetrical porphyrin units through nucleophilic addition. The carbonyl groups in para position of BDA serve as the knot to connect the porphyrin units through benzene linkages to construct the 2D framework structure of POF. Experimentally, stoichiometric pyrrole and BDA were solved in propionic acid with trifluoroacetic acid (TFA) as the catalyst and nitrobenzene (NBZ) as the oxidant. The mixture was simply kept at 130 °C for 12.0 h under continuous stirring to afford black solid products. After routine filtration and washing, 2.17 g POF was finally obtained with a yield as high as 95%.

2. Results and Discussion

The morphology of POF was characterized by a scanning electron microscope (SEM) and a transmission electron microscope (TEM). The as-synthesized POF exhibits a uniform sphere morphology with an average diameter of 1.0 μm (Figure S2, Supporting Information). High-resolution TEM images (Figure S3, Supporting Information) demonstrate a typical flake-like structure at the edge of the POF spheres, indicating its intrinsic 2D structure. After simple sonication, however, large POF sheets were unambiguously observed (**Figure 2A**) to reveal the 2D nature of POF. The POF sheets stack as a layered structure with an interlayer spacing of 0.39 nm (Figure 2B). Atomic force microscope (AFM) images in Figure 2C and Figure S4 (Supporting Information) further demonstrate the POF sheets are $\approx 5 \mu\text{m}$ in width and around 4 nm in thickness. The layer number is calculated to be about ten. The above morphology characterizations evidently prove POF as a typical 2D material endowed by its unique framework structure.

The chemical structure of POF was first investigated using Fourier transform infrared spectrometry (FTIR). As demonstrated in Figure S5 (Supporting Information), the adsorption band of carbonyl groups at 1700 cm^{-1} is greatly reduced in POF, indicating full conversion of the BDA precursor. The C=C and C=N stretching vibrations of POF give rise to the adsorption bands from 1600 to 1400 cm^{-1} ,^[19] and the adsorption bands at around 1250, 1000, and 800 cm^{-1} are assigned to C–N vibrations, C–H vibrations, and in-plane porphyrin deformation modes, respectively.^[20] Solid-state ^1H and ^{13}C nuclear magnetic resonance (NMR) spectra of POF further confirm successful construction of the porphyrin structure. Peaks of the ^{13}C NMR

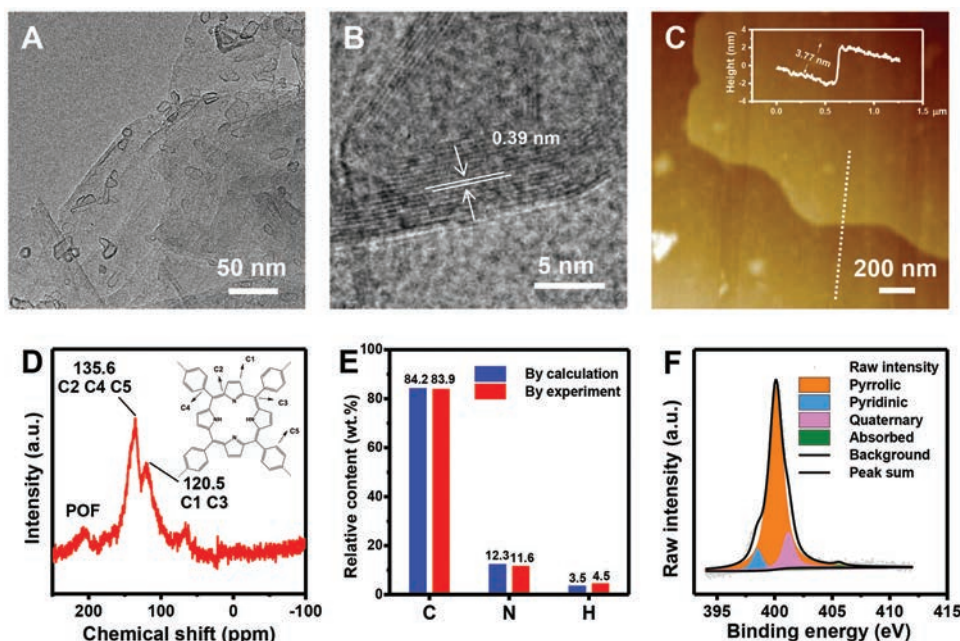


Figure 2. Morphology and structure characterization of POF. A) TEM image, B) high-resolution TEM image, and C) AFM image of POF. The inset graph in (C) is the corresponding height profile where the dashed line marks the position for height measurements. D) Solid-state ^{13}C NMR spectrum of POF. The inset in (D) is the corresponding structural identification. E) Elemental relative content of POF by theoretical calculation and by experimental combustion method. F) High-resolution N 1s XPS spectrum of POF. The N content of POF is dominant pyrrolic N, which agrees with the pyrrole precursor.

spectrum at 120.5 and 135.6 ppm are assigned to the porphyrin and benzene linkages (Figure 2D).^[21] The ¹H NMR spectrum affords three peaks and is in consistency with three kinds of hydrogen environments in the POF structure (Figure S6, Supporting Information). In addition, the strong ultraviolet–visible (UV–vis) absorbance of POF above 300 nm indicates the formation of a highly conjugated structure, suggesting successful construction of the porphyrin structure as a side evidence (Figure S7, Supporting Information). Elemental contents of POF were comprehensively analyzed by the combustion method (COM), energy-dispersive X-ray spectrometer (EDS), and X-ray photoelectron spectroscopy (XPS). POF exhibits a reasonable N content of 11.6 wt% determined by COM, which is close to the theoretical value of 12.3 wt% (Figure 2E). No O content was detected by EDS (Figure S8A, Supporting Information), implying the completeness of POF synthesis by fully dehydration. High-resolution N 1s XPS spectrum in Figure 2F indicates the N content is dominant pyrrolic N at 400.1 eV with negligible pyridinic N (398.5 eV), quaternary N (401.2 eV), or adsorbed N (405.6 eV).^[22] The evidence agrees with the pyrrole substrate, which remains stable during POF synthesis.

The SSA of POF is determined to be 303 cm² g⁻¹ using the multipoint Brunauer–Emmett–Teller (BET) method (Figure S9A, Supporting Information), and the pore volume is 0.303 cm³ g⁻¹ based on the quenched solid density functional theory (Figure S9B, Supporting Information). The pore-size distribution exhibits a unique micropore structure dominating at 1.4 nm and multiple mesopore structures at 4.2 and 6.8 nm, respectively. The micropore structure is ascribed as the characteristic pore structure of POF materials.

We further applied X-ray diffraction (XRD) to elucidate the structure of POF. The as-synthesized POF exhibits an obvious diffraction peak at 13°, suggesting the intrinsic ordered structure of POF distinguished from amorphous polymers (Figure S10A, Supporting Information). After sonication of the as-synthesized POF, however, POF reveals its crystallized nature and ordered structure by offering sharp diffraction peaks (Figure S10B, Supporting Information). First-principles calculations were performed to determine the crystal structure of POF. As exhibited in Figure S11A (Supporting Information), POF affords a layered structure of tetragonal sheets. The stacking of POF is staggered along the *a*-axis, which is caused by the intermolecular repulsion among the rotated benzene rings between the POF layers and induces a slight difference between the sizes of the *a* and *b*-axes. The average layer spacing of POF is 3.90 Å (Figure S11B, Supporting Information), which agrees with the TEM results. The simulated XRD patterns are consistent with the experimental results by affording identical diffraction peaks (Figure S11C, Supporting Information). The XRD peaks at 11° and 22° of POF are assigned to the diffraction of (101) and (002) crystal faces accordingly. In addition, the theoretical predicted pore size of 1.3 nm in diameter matches with the experimental results that identify the 1.4 nm micropore as the intrinsic pore structure of POF (Figure S11D, Supporting Information).

Although the structure of POF is definite, the changes of the XRD patterns of POF after sonication remain unclear. Considering the intrinsically ordered structure of POF, we hypothesize the wide peaks of the as-synthesized POF are generated by random stacking of POF layers. Such disorder

lowers the overall crystallinity and offers wide diffraction peaks. With the energy provided by sonication, the POF layers stack back into ordered structure as the stable thermodynamic product. Consequently, the stable crystallized POF offers intense XRD peaks.

In order to prove the above hypothesis, molecular dynamics (MD) simulations were performed. Sixteen POF layers composed of 16 porphyrin units (4 × 4) were randomly placed in a 20 nm cell and three different initial patterns were considered (Figure S12A–C, Supporting Information). The systems went through a 4.0 ns MD process to arrive at a stable structure. As expected, the 16 POF layers were spontaneously stacked with each other to form a super layer in three systems (Figure S12D–F, Supporting Information). Comparing the simulated XRD patterns of the initial and final POF (Figure S12G–I, Supporting Information), only the intrinsic peaks at low angles are retained. Multiple peaks at higher angles are either decayed or disappeared, corresponding to the spontaneous formation of ordered POF structure. Considering abundant cells composed of randomly dispersed POF layers describing the as-synthesized POF, such a system generates multiple diffraction peaks and exhibits an overall wide peak in spite of the well-defined POF structure. After sonication treatment, the POF system returned to a stable stacking structure and consequently the intense intrinsic diffraction peaks were revealed.

With the successful synthesis of POF, we further attempt to regulate the morphology of POF to reveal its diversity. One effective method for morphology regulation is to introduce suitable templates for in situ growth.^[23] Herein, copper foil (CF) is selected as a macrotemplate because it is stable against acid and heat during POF synthesis. Interestingly, POF spreads itself on the surface of CF to afford a homogeneous free-standing POF film (POF-F). The areal density of the POF-F is ≈0.3 mg cm⁻². The macrograph in Figure 3A demonstrates a POF-F on a silicon substrate. POF-F appears as a black sheet of several centimeters in width. As shown in Figure S13 (Supporting Information), POF-F can be transformed onto various templates such as Al foil, Cu foil, and glass. In addition, POF-F can be easily dispersed in ethanol (Figure S13D, Supporting Information), making it easy and convenient for manipulating free-standing POF-F and bulk transfer.

SEM images of POF-F (Figure S14, Supporting Information) exhibit a rugged morphology, which is in replication of the CF template. The layered structure of POF-F indicated by TEM images (Figure S15, Supporting Information) is inherited from the intrinsic 2D structure of POF. Estimated by the thickness determined by the AFM characterization (Figure 3B), about 100 POF layers were packed with each other into a 2D POF-F.

Furthermore, POF renders excellent compatibility with a family of macro/microscale templates. Herein, graphene (G) was applied as the template for POF hybridization because of its 2D structure and unique characters in both physical and chemical aspects.^[24] Graphene is introduced to POF synthesis by mixing with the precursors under sonication, and the hybridized material is named as G@POF. In contrast to clean 2D graphene nanosheets (Figure S16, Supporting Information), POF was uniformly deposited on the graphene template, attributing to the intermolecular π – π interaction between POF and G (Figure 3C). Neither POF sphere nor other segregate POF

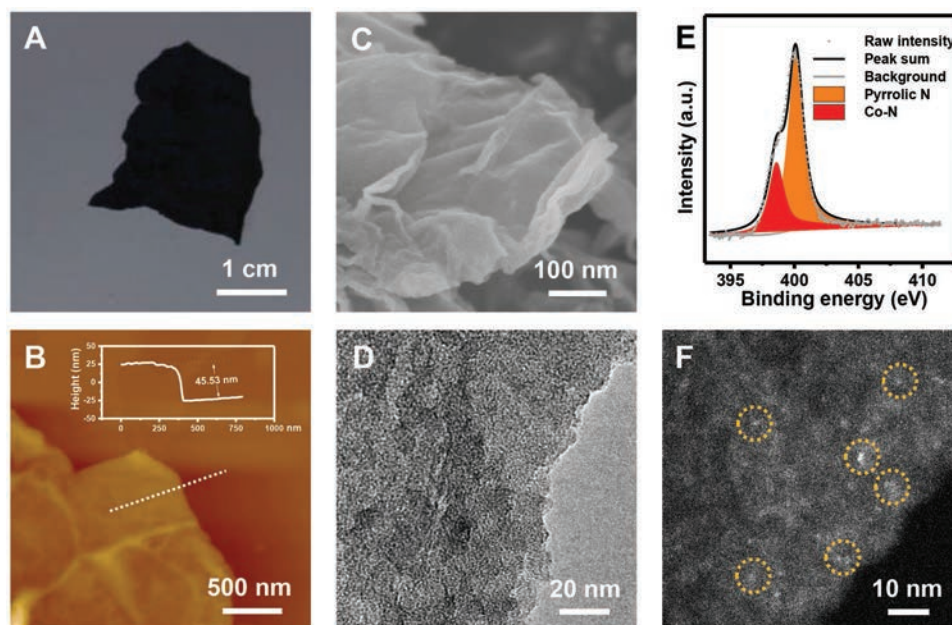


Figure 3. Characterization of template-synthesized POF. A) Macrograph of POF-F on a silicon substrate. B) AFM image and inserted corresponding height profile of POF-F. C) SEM image and D) TEM image of G@POF. E) High-resolution N 1s XPS spectrum of G@POF-Co. F) HAADF-STEM image of G@POF-Co. The bright dots highlighted with yellow circles are ascribed as the Co content that is uniformly distributed on the surface of G@POF-Co.

is observed (Figure S17A, Supporting Information), suggesting POF is dominantly hybridized with graphene. TEM images in Figure 3D and Figure S15 (Supporting Information) indicate a unique scaly morphology of G@POF. The G@POF sheets are neat and uniform, with the POF flakes spreading on the surface of graphene. The SSA of G@POF increases to $541 \text{ m}^2 \text{ g}^{-1}$ compared with POF as a result of hybridization with G (SSA = $614 \text{ m}^2 \text{ g}^{-1}$) (Figure S18A, Supporting Information). The pore-size distribution of G@POF is otherwise identical to G except for the micropores at 1.4 nm (Figure S18B, Supporting Information), which is assigned as the intrinsic pore structure of POF in agreement with the simulated results. The hybridization of G@POF unfolds the stacked POF layers onto graphene surface, offering abundant surface functional groups as active sites.

FTIR spectra (Figure S19, Supporting Information) provide direct evidence of POF hybridized with graphene. The adsorption band at 1600 cm^{-1} of graphene is assigned as the stretching vibration of C=C, while the band is shifted to higher frequency because of the existence of C=N bonds of POF.^[25] XRD patterns in Figure S20 (Supporting Information) afford an obvious POF peak as a verification while the diffraction peaks of graphene are distinguished at higher degrees assigned as (002) and (100) crystal faces, respectively.^[26] Elemental analysis further probes the hybridization of POF with graphene (Figure S21, Supporting Information). G@POF exhibits an evident N content of 6.9 at% by XPS. In contrast, no N content was detected on G. High-resolution N 1s XPS spectrum in Figure S22 (Supporting Information) further indicates the dominant pyrrolic N content of G@POF similar with POF.

To probe POF as a functional material for practical applications, we applied POF as an electrocatalyst for oxygen reduction reaction (ORR) and oxygen evolution reaction (OER). ORR and OER constitute the core process of many sustainable energy

devices such as fuel cells, rechargeable metal–air batteries, and water splitting techniques.^[27] However, both ORR and OER are kinetically unfavorable and electrocatalysts are strongly demanded.^[28] Noble-metal-based electrocatalysts possess excellent ORR/OER reactivity. However, the scarcity and high cost of noble metal limit their applications in practical systems.^[29] Noble-metal-free electrocatalysts are highly concerned for ORR and OER recently.^[30]

The superior performance for oxygen electrocatalysis has been reported on porphyrin-based materials.^[21a,31] For instance, cobalt porphyrin multilayers on reduced graphene oxides demonstrate promising ORR reactivity.^[32] In addition, Lin et al. provided theoretical evidence that porphyrin units possess ORR and OER bifunctions.^[33] Inspired by these works, we applied Co^{2+} coordinated POF hybridized with G as an emerging electrocatalyst for ORR and OER, which is named as G@POF-Co herein. The porphyrin coordinated with Co^{2+} serves as active sites while graphene affords electrical conductivity and highly exposed surface. G@POF-Co was fabricated using otherwise identical methods as G@POF except with $\text{Co}(\text{CH}_3\text{COO})_2$ added as the Co source.

Verified by FTIR spectrum in Figure S23 (Supporting Information) and XRD patterns in Figure S24 (Supporting Information), POF was sufficiently hybridized with graphene, with elemental analysis in Figure S25 (Supporting Information) affording reasonable N content of G@POF-Co compared with G@POF. The Co content is unambiguously detected by both EDS and XPS, with a bulk and surface Co content being 2.0 at% and 0.6 at%, respectively. Both pyrrolic N at 400.1 eV and Co–N at 398.5 eV were observed on the high-resolution N 1s XPS spectrum (Figure 3E).^[13,21a] The Co–N peak provides strong evidence of coordinated porphyrin with Co^{2+} in G@POF-Co. Further high-resolution Co 2p XPS spectrum (Figure S26,

Supporting Information) confirms that cobalt ions are in +2 oxidation state without the formation of Co nanoparticles.^[34] Co-coordinated porphyrin units are successfully linked as stable 2D frameworks for further electrocatalysis.

The morphology of G@POF-Co is similar to G@POF with scaly POF flakes on the surface of graphene (Figure S27, Supporting Information). High-angle annular dark-field scanning transmission electron microscopy (HAADF-STEM) image (Figure 3F) reveals punctate contrast that is ascribed as the Co content. The SSA and pore volume of G@POF-Co remain $460 \text{ m}^2 \text{ g}^{-1}$ and $1.69 \text{ cm}^3 \text{ g}^{-1}$, respectively, with a similar pore-size distribution as G@POF (Figure S28, Supporting Information). The well-dispersed Co-coordinated porphyrin units uniformly spread on graphene surface are expected to fully demonstrate the reactivity of G@POF-Co for bifunctional oxygen electrocatalysis.

Electrochemical characterization of G@POF-Co was carried out. Commercial 20% Pt/C was used as the benchmark to evaluate the ORR performance of G@POF-Co. The areal loading of all electrocatalysts is 0.10 mg cm^{-2} . As shown in the linear sweep voltammetry (LSV) profiles of ORR, G@POF-Co affords an ORR on-set potential of 0.87 V versus reversible hydrogen electrode (RHE) (Figure 4A) in 0.10 M KOH electrolyte. Half-wave potential ($E_{1/2}$) to reach a current density of 2.5 mA cm^{-2} is considered as the indicator of ORR reactivity.^[35] The $E_{1/2}$ of G@POF-Co is 0.81 V versus RHE, which is close to the state-of-the-art Pt/C electrocatalyst of $E_{1/2} = 0.85 \text{ V}$ versus RHE. Decreased Tafel slopes in Figure 4B further imply superior kinetics of G@POF-Co (46.9 mV dec^{-1}) over Pt/C (88.2 mV dec^{-1}). Graphene, however, is not reactive for ORR with lower $E_{1/2}$ and higher Tafel slope (Figure S29, Supporting Information).

The reduction of O_2 is through either a two-electron pathway to produce peroxide or a four-electron pathway to produce water.^[28] As demonstrated in Figure S30 (Supporting Information), G@POF-Co performs as a typical four-electron ORR electrocatalyst comparable with Pt/C with an electron transfer number (n) being 3.8 over a voltage range from 0.8 to 0.1 V versus RHE in alkaline electrolyte, while graphene exhibits a mixed ORR pathway. G@POF-Co offers a clear pathway for full reduction of O_2 .

Figure S31 (Supporting Information) demonstrates the durability response of G@POF-Co and Pt/C in alkaline electrolyte. G@POF-Co remained a current density of 84% after 30 000 s while only 65% of the current density was left for Pt/C. G@POF-Co also exhibits desirable durability against methanol, a common intermediate in fuel cells, with no decay in current density when methanol is added (Figure S32, Supporting Information). However, Pt/C was poisoned by methanol with the current density being decreased significantly.^[36] G@POF-Co exhibits comparable reactivity, faster kinetics, and superior stability over Pt/C and serves as a promising electrocatalyst for ORR.

LSV profiles in Figure S33A (Supporting Information) demonstrate the OER performance of G, G@POF-Co, and IrO_2 as the benchmark electrocatalyst. The overpotential at 10.0 mA cm^{-2} (η_{10}) is used to evaluate the reactivity of OER.^[37] G@POF-Co exhibits a η_{10} of 430 mV, only 30 mV higher than the state-of-the-art IrO_2 electrocatalyst and much better than G. Tafel slopes in Figure S33B (Supporting Information) indicate the kinetics of OER is slower for G@POF-Co of 161 mV dec^{-1} beneath IrO_2 of 87.9 mV dec^{-1} .

Bifunctional performance for ORR and OER is of great significance in secondary energy storage devices. The potential gap (ΔE) between the ORR half-wave potential ($E_{1/2}$) and the

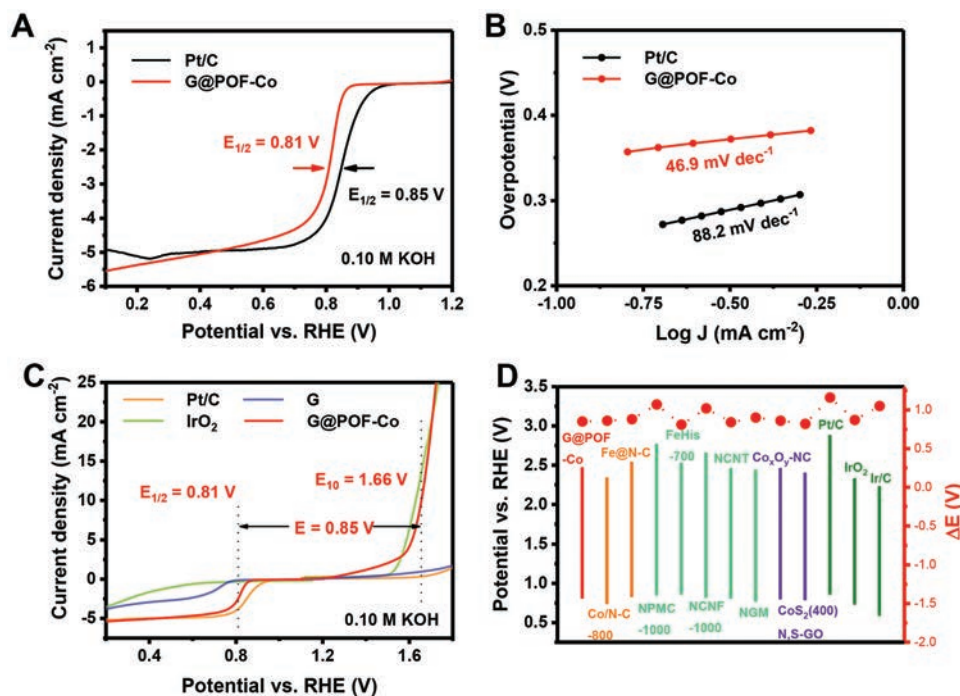


Figure 4. Electrochemical performance in O_2 -saturated 0.10 M KOH electrolyte. A) 95% iR -compensated LSV profiles of Pt/C and G@POF-Co at a scan rate of 10.0 mV s^{-1} for ORR and B) corresponding Tafel plots. C) 95% iR -compensated ORR and OER LSV profiles of Pt/C, IrO_2 , G, and G@POF-Co for bifunctional performance evaluation. D) Comparison of ORR/OER bifunctional performance of the recent reported electrocatalysts.

potential required at an OER current density of 10.0 mA cm^{-2} ($E_{j=10}$) is used as the indicator to evaluate the bifunctional performance.^[22a,38] G@POF-Co exhibits a ΔE of 0.85 V (Figure 4C) and is among the best noble-metal-free bifunctional electrocatalysts in alkaline electrolyte (Figure 4D). Furthermore, the as-synthesized POF was exposed in atmosphere for 3 months to evaluate its durability. The dated G@POF-Co (named as d-G@POF-Co) demonstrates scarcely decayed performances for both ORR and OER (Figure S34, Supporting Information). $E_{1/2}$ of d-G@POF-Co is only 20 mV lower with η_{10} being increased by 30 mV. Therefore, G@POF-Co serves as a superb electrocatalyst for ORR and OER.

3. Conclusion

In conclusion, we synthesized POF as an emerging family of organic framework materials. The direct synthesis methodology was proposed as a guidance for optimizing the substrate selection, the synthesis routine, and the function. One-pot synthesis of the POF materials was achieved with high quality, output, and yield. The as-synthesized POF materials are intrinsic 2D and reveal impressive versatility in composition, structure, morphology, and function. G@POF-Co serves as a model POF material to demonstrate excellent ORR and OER reactivity for practical applications, with comparable bifunctional performances among the best. POF presents the ability to synthesis and control materials at the atomic level. More molecular materials are coming from the POF family to serve as an emerging platform to demonstrate their advances in chemistry and material sciences for sustainable world.

4. Experimental Section

Synthesis of POF: POF was synthesized by a simple one-pot method. BDA (1.34 g, 10 mmol) was first solved into 100 mL propionic acid by stirring for 10 min. To the solution were added 1.0 mL TFA and 5.0 mL NBZ as the catalyst and the oxidant. After that, pyrrole (1.39 mL, 20 mmol) was added drop wise into the above solution under stirring, which turned into deep purple. The mixture was kept at 130 °C under continuous stirring for 12 h and cooled to room temperature overnight to afford a dark suspension. The product was filtered and washed with ethanol, chloroform, and ethanol to remove unreacted reagents and small porphyrin molecules. POF was finally obtained as black powders after being dried at 60 °C for 24 h. The yield was calculated based on the actual and theoretical output of POF using the following equation

$$\text{yield} = m_{\text{POF}} / (M_{\text{POF}} \times n_{\text{POF}}) \times 100\% \quad (1)$$

where m_{POF} is the actual output of POF determined by measuring the mass of the synthesized POF, M_{POF} is the molar mass of POF based on the formula of $(\text{C}_{32}\text{H}_{18}\text{N}_4)_m$, and n_{POF} is the amount of POF determined by the POF substrates. The actual output of POF is 2.17 g and the yield is 95% according to the above method.

The sonication of POF was carried out according to the following method: 10 mg of POF was dispersed into 5.0 mL ethanol to form a homogeneous suspension. The suspension was then sonicated for 30 min and centrifuged at a rotating speed of 2000 rpm for 10 min. The supernatant and the sediment were kept separately for further characterization.

Synthesis of POF-F: POF-F was fabricated using a similar method as POF with CF as template. Typically, CF (5 cm × 5 cm) was added into a 50 mL acetic acid solution of BDA (27 mg, 0.2 mmol), pyrrole (28 μL ,

0.4 mmol), TFA (0.10 mL), and NBZ (0.50 mL). The mixture was kept at 80 °C for 24 h without stirring and then cooled to room temperature. Black POF sheets were picked from the resulting suspension and purified by soaking into ethanol, chloroform, and ethanol for 1.0 h, respectively. After drying at 60 °C for 24 h, POF-F was fabricated for further characterization.

Synthesis of G@POF: G@POF was synthesized through otherwise identical methods as POF with G added as the template. G was fabricated by reducing graphene oxide at high temperature, and more details can be found in our previous publication.^[39] Particularly, 750 mg G was added into the propionic acid solution of BDA, TFA, and NBZ with the same concentration as POF synthesis. The theoretical mass ratio of G:POF was calculated to be 1:3. The slurry was then sonicated for 30 min for intensive mixing of G and the reactants. After pyrrole was added, the mixture was kept at 130 °C for 12 h under continuous stirring. G@POF was finally obtained after purification and drying using the same methods as POF. The yield of G@POF was 97%.

Synthesis of G@POF-Co: G@POF-Co was synthesized and purified using similar procedures as G@POF with Co^{2+} introduced as the central ion coordinated within porphyrin rings. Cobalt acetate ($\text{Co}(\text{CH}_3\text{COO})_2$, 6.2 g, 25 mmol) was added after pyrrole and the mixture was stirred for another 10 min for intensive solvation. The molar ratio of Co^{2+} to porphyrin unit was 5:1 to guarantee the coordination. The yield of G@POG-Co was 98%.

Structural Characterization: FTIR was carried out using a NEXUS 870 spectrograph. UV-vis absorption spectrum was obtained on a Hitachi U-3010 Spectrophotometer. XRD patterns were recorded on a Bruker D8 Advanced diffractometer with $\text{Cu-K}\alpha$ radiation at 40.0 kV and 120 mA. XPS measurements were performed by Escalab 250xi. All XPS spectra were corrected using carbon 1s line at 284.6 eV. Solid-state ^1H and ^{13}C dipolar-decoupling Magic Angle Spinning NMR spectra were collected using a JNM-ECZ600R at 600 MHz with a rotating speed of 10 kHz and a relaxation time of 5.0 s. The nitrogen adsorption-desorption isotherm was collected at 77 K using an Autosorb-IQ2-MP-C system. All samples were degassed at 200 °C for 10.0 h before physisorption measurements. Multipoint BET method was applied to determine the SSA. The pore-size distribution was calculated using the quenched solid density functional theory based on the data of the adsorption branch. Elemental analysis was performed using combustion method on an elemental analyzer (Vario El III, Germany) under O_2 flow at 1000 °C. The macrographs were recorded using a Canon camera. The morphology of the samples was characterized using a JSM 7401F (JEOL Ltd., Tokyo, Japan) SEM at 3.0 kV and a JEM 2010 (JEOL Ltd., Tokyo, Japan) TEM at 120.0 kV. EDS analysis was carried out on the JEM 2010 TEM equipped with an Oxford Instrument energy dispersive X-ray spectrometer. HAADF-STEM images were recorded on an FEI Tecnai G² F20 TEM. AFM images were obtained using a NanoMan scanning probe microscope with a NanoScope V controller.

Electrochemical Evaluation: The electrochemical characterization was carried out using a three-electrode system controlled by a CHI 760E electrochemistry station (CH Instrument, USA). The counter electrode was a platinum sheet electrode and a saturated calomel electrode (SCE) served as the reference electrode. The working electrode was a rotating ring-disk electrode. The disk electrode was glass carbon with a diameter of 5.0 mm, and the ring electrode was platinum with an inner diameter of 6.5 mm and an outer diameter of 7.5 mm.

Fabrication of the working electrode was performed using the following method: 5.0 mg electrocatalyst and 1.0 mg carbon nanotube (CNT) were dispersed into 0.95 mL ethanol and 0.05 mL Nafion solution (5.0 wt%). CNT was added to enhance the conductivity of the samples. The mixture was then sonicated for 30 min to afford a homogeneous suspension. 4.0 μL of the suspension was dropped onto the disk electrode, which was polished and washed under sonication in advance. After the solvent was evaporated, the working electrode was ready for electrochemical evaluation. The areal loading mass of the working electrode was 0.10 mg cm^{-2} for the electrocatalysts. The areal loading mass of benchmark Pt/C and IrO_2 electrocatalysts is equally 0.10 mg cm^{-2} for comparison.

All the electrochemical measurements were conducted in O₂-saturated 0.10 mol L⁻¹ KOH electrolyte at room temperature. The rotating speed of the working electrode was 1600 rpm during the tests. All potentials recorded were corrected to RHE according to the following equation: $E_{\text{RHE}} = E_{\text{SCE}} + 0.241 \text{ V} + 0.0592 \text{ pH}$. All samples were stabilized by cyclic voltammetry at a scan window from 0.00 to 2.00 V versus SCE before electrochemical measurements.

The ORR and OER reactivity of the electrocatalysts was evaluated using LSV at a scan rate of 10.0 mV s⁻¹ with the scan window determined according to the tested reaction. All polarized profiles were corrected with 95% *iR*-compensation. During the ORR LSV tests, the ring electrode was set at a constant potential of 0.50 V versus SCE to detect the peroxide intermediates. The electron transfer number *n* was then calculated based on the current of the disk and the ring electrode using the following equation

$$n = 4I_d / (I_d + I_r / N) \quad (2)$$

where I_d is the disk current, I_r is the current for ring electrode, and *N* is the current collection efficiency of the ring electrode that was determined to be 0.26 in this case.

The kinetics of the electrocatalysts were characterized by Tafel slopes. Tafel slopes were calculated based on the LSV profiles using the Tafel equation: $\eta = b \log(j/j_0)$. Among them, η is the overpotential calculated by $\eta = |E_{\text{RHE}} - 1.23 \text{ V}|$, *j* is the disk current density, j_0 is the exchange current density, and *b* is the Tafel slope.

The stability of the electrocatalysts against ORR was evaluated at a constant voltage required to reach an initial current density of 2.5 mA cm⁻².

Computational Details: The first-principles calculations were conducted in Vienna Ab initio Simulation Package (VASP)^[40] and the results were visualized in Materials Studio. The projector augmented-wave^[41] pseudopotentials and Perdew–Burke–Ernzerhof generalized-gradient approximation functional^[42] were adopted in all density functional theory (DFT) calculations. The energy cutoff was set to 520 eV. The self-consistent field (SCF) and geometry convergence tolerance were set to 1×10^{-5} and 1×10^{-4} eV, respectively. Particularly, the van der Waals interaction was described with DFT-D3 method^[43] as physical interaction takes an important role in 2D materials simulations.

The MD simulations were conducted in the Forcite module of Materials Studio. The microcanonical ensemble (NVE) ensemble with a fixed temperature of 298 K was adopted. The time step was set to 1.0 fs and a 4 000 000-step simulation (4 ns) was performed. Besides, a universal force field was adopted during the MD simulations.

The XRD simulations were conducted in the Reflex Powder Diffraction module of Materials Studio.

Supporting Information

Supporting Information is available from the Wiley Online Library or from the author.

Acknowledgements

This work was supported by the National Key Research and Development Program (2016YFA0202500 and 2016YFA0200102), the National Natural Scientific Foundation of China (21825501), the Tsinghua University Initiative Scientific Research Program, and the Tsinghua National Laboratory for Information Science and Technology. The authors thank Dr. Cheng Tang, Dr. Hong-Jie Peng, Jia-Ning Liu, Jin Xie, and Prof. Jia-Qi Huang for helpful discussion.

Conflict of Interest

The authors declare no conflict of interest.

Keywords

2D materials, bifunctional oxygen electrocatalysts, framework porphyrin, one-pot synthesis, oxygen reduction reaction

Received: February 12, 2019

Revised: March 30, 2019

Published online:

- [1] a) A. K. Geim, K. S. Novoselov, *Nat. Mater.* **2007**, *6*, 183; b) A. P. Alivisatos, *Science* **1996**, *271*, 933.
- [2] a) C. S. Diercks, O. M. Yaghi, *Science* **2017**, *355*, eaal1585; b) O. M. Yaghi, M. O’Keeffe, N. W. Ockwig, H. K. Chae, M. Eddaoudi, J. Kim, *Nature* **2003**, *423*, 705; c) A. P. Cote, H. M. El-Kaderi, H. Furukawa, J. R. Hunt, O. M. Yaghi, *J. Am. Chem. Soc.* **2007**, *129*, 12914.
- [3] a) S. Y. Ding, W. Wang, *Chem. Soc. Rev.* **2013**, *42*, 548; b) N. Huang, P. Wang, D. L. Jiang, *Nat. Rev. Mater.* **2016**, *1*, 16068.
- [4] A. P. Cote, A. I. Benin, N. W. Ockwig, M. O’Keeffe, A. J. Matzger, O. M. Yaghi, *Science* **2005**, *310*, 1166.
- [5] a) P. Kuhn, A. Forget, D. S. Su, A. Thomas, M. Antonietti, *J. Am. Chem. Soc.* **2008**, *130*, 13333; b) J. Mahmood, E. K. Lee, M. Jung, D. Shin, I. Y. Jeon, S. M. Jung, H. J. Choi, J. M. Seo, S. Y. Bae, S. D. Sohn, N. Park, J. H. Oh, H. J. Shin, J. B. Baek, *Nat. Commun.* **2015**, *6*, 6486; c) Y. X. Ma, Z. J. Li, L. Wei, S. Y. Ding, Y. B. Zhang, W. Wang, *J. Am. Chem. Soc.* **2017**, *139*, 4995.
- [6] a) C. E. Chan-Thaw, A. Villa, P. Katekomol, D. S. Su, A. Thomas, L. Prati, *Nano Lett.* **2010**, *10*, 537; b) S. Lin, C. S. Diercks, Y. B. Zhang, N. Kornienko, E. M. Nichols, Y. B. Zhao, A. R. Paris, D. Kim, P. Yang, O. M. Yaghi, C. J. Chang, *Science* **2015**, *349*, 1208.
- [7] a) Z. A. Ghazi, L. Y. Zhu, H. Wang, A. Naeem, A. M. Khattak, B. Liang, N. A. Khan, Z. X. Wei, L. S. Li, Z. Y. Tang, *Adv. Energy Mater.* **2016**, *6*, 1601250; b) V. S. Vyas, F. Haase, L. Stegbauer, G. Savasci, F. Podjaski, C. Ochsenfeld, B. V. Lotsch, *Nat. Commun.* **2015**, *6*, 8508; c) S. Wang, Q. Y. Wang, P. P. Shao, Y. Z. Han, X. Gao, L. Ma, S. Yuan, X. J. Ma, J. W. Zhou, X. Feng, B. Wang, *J. Am. Chem. Soc.* **2017**, *139*, 4258; d) P. Peng, Z. Zhou, J. Guo, Z. Xiang, *ACS Energy Lett.* **2017**, *2*, 1308.
- [8] a) N. Huang, X. Chen, R. Krishna, D. L. Jiang, *Angew. Chem., Int. Ed.* **2015**, *54*, 2986; b) M. G. Rabbani, H. M. El-Kaderi, *Chem. Mater.* **2011**, *23*, 1650.
- [9] S. Y. Ding, J. Gao, Q. Wang, Y. Zhang, W. G. Song, C. Y. Su, W. Wang, *J. Am. Chem. Soc.* **2011**, *133*, 19816.
- [10] K. Wang, L.-M. Yang, X. Wang, L. Guo, G. Cheng, C. Zhang, S. Jin, B. Tan, A. Cooper, *Angew. Chem., Int. Ed.* **2017**, *56*, 14149.
- [11] T. Ben, H. Ren, S. Ma, D. Cao, J. Lan, X. Jing, W. Wang, J. Xu, F. Deng, J. M. Simmons, S. Qiu, G. Zhu, *Angew. Chem., Int. Ed.* **2009**, *48*, 9457.
- [12] S. Kandambeth, V. Venkatesh, D. B. Shinde, S. Kumari, A. Halder, S. Verma, R. Banerjee, *Nat. Commun.* **2015**, *6*, 6786.
- [13] S. Bruller, H. W. Liang, U. I. Kramm, J. W. Krumpfer, X. L. Feng, K. Mullen, *J. Mater. Chem. A* **2015**, *3*, 23799.
- [14] X. Chen, M. Addicoat, E. Q. Jin, L. P. Zhai, H. Xu, N. Huang, Z. Q. Guo, L. L. Liu, S. Irlle, D. L. Jiang, *J. Am. Chem. Soc.* **2015**, *137*, 3241.
- [15] a) M. J. Climent, A. Corma, S. Iborra, *Chem. Rev.* **2011**, *111*, 1072; b) Z. Y. Zhang, I. R. Ollmann, X. S. Ye, R. Wischnat, T. Baasov, C. H. Wong, *J. Am. Chem. Soc.* **1999**, *121*, 734.
- [16] a) H. P. Liao, H. M. Wang, H. M. Ding, X. S. Meng, H. Xu, B. S. Wang, X. P. Ai, C. Wang, *J. Mater. Chem. A* **2016**, *4*, 7416; b) H. Sahabudeen, H. Y. Qi, B. A. Glatz, D. Tranca, R. H. Dong, Y. Hou, T. Zhang, C. Kuttner, T. Lehnert, G. Seifert, U. Kaiser, A. Fery, Z. K. Zheng, X. L. Feng, *Nat. Commun.* **2016**, *7*, 13461; c) V. Netti, X. F. Wu, S. G. Deng, L. Echegoyen, *Polym. Chem.* **2013**, *4*, 4566.

- [17] B. Sun, J. Li, W. L. Dong, M. L. Wu, D. Wang, *J. Phys. Chem. C* **2016**, 120, 14706.
- [18] a) A. D. Adler, W. Shergilas, F. R. Longo, *J. Am. Chem. Soc.* **1964**, 86, 3145; b) P. Rothmund, *J. Am. Chem. Soc.* **1936**, 58, 625.
- [19] L. J. Boucher, J. J. Katz, *J. Am. Chem. Soc.* **1967**, 89, 1340.
- [20] D. W. Thomas, A. E. Martell, *J. Am. Chem. Soc.* **1959**, 81, 5111.
- [21] a) Z. S. Wu, L. Chen, J. Z. Liu, K. Parvez, H. W. Liang, J. Shu, H. Sachdev, R. Graf, X. L. Feng, K. Mullen, *Adv. Mater.* **2014**, 26, 1450; b) S. Wan, F. Gandara, A. Asano, H. Furukawa, A. Saeki, S. K. Dey, L. Liao, M. W. Ambrogio, Y. Y. Botros, X. Duan, S. Seki, J. F. Stoddart, O. M. Yaghi, *Chem. Mater.* **2011**, 23, 4094.
- [22] a) C. Tang, H. F. Wang, X. Chen, B. Q. Li, T. Z. Hou, B. S. Zhang, Q. Zhang, M. M. Titirici, F. Wei, *Adv. Mater.* **2016**, 28, 6845; b) S. Biniak, G. Szymanski, J. Siedlewski, A. Swiatkowski, *Carbon* **1997**, 35, 1799; c) D. H. Guo, R. Shibuya, C. Akiba, S. Saji, T. Kondo, J. Nakamura, *Science* **2016**, 351, 361.
- [23] a) C. Tang, B. Q. Li, Q. Zhang, L. Zhu, H. F. Wang, J. L. Shi, F. Wei, *Adv. Funct. Mater.* **2016**, 26, 577; b) M. Q. Zhao, Q. Zhang, J. Q. Huang, G. L. Tian, J. Q. Nie, H. J. Peng, F. Wei, *Nat. Commun.* **2014**, 5, 3410.
- [24] a) L. R. Xu, X. Zhou, W. Q. Tian, T. Gao, Y. F. Zhang, S. B. Lei, Z. F. Liu, *Angew. Chem., Int. Ed.* **2014**, 53, 9564; b) J. W. Colson, A. R. Woll, A. Mukherjee, M. P. Levendorf, E. L. Spitler, V. B. Shields, M. G. Spencer, J. Park, W. R. Dichtel, *Science* **2011**, 332, 228.
- [25] C. Zhang, D. M. Dabbs, L. M. Liu, I. A. Aksay, R. Car, A. Selloni, *J. Phys. Chem. C* **2015**, 119, 18167.
- [26] a) S. Dubin, S. Gilje, K. Wang, V. C. Tung, K. Cha, A. S. Hall, J. Farrar, R. Varshneya, Y. Yang, R. B. Kaner, *ACS Nano* **2010**, 4, 3845; b) H. K. Jeong, Y. P. Lee, M. H. Jin, E. S. Kim, J. J. Bae, Y. H. Lee, *Chem. Phys. Lett.* **2009**, 470, 255.
- [27] a) S. Chu, Y. Cui, N. Liu, *Nat. Mater.* **2017**, 16, 16; b) J. T. Zhang, Z. H. Zhao, Z. H. Xia, L. M. Dai, *Nat. Nanotechnol.* **2015**, 10, 444.
- [28] Y. Jiao, Y. Zheng, M. T. Jaroniec, S. Z. Qiao, *Chem. Soc. Rev.* **2015**, 44, 2060.
- [29] a) N. Zhang, Y. G. Feng, X. Zhu, S. J. Guo, J. Guo, X. Q. Huang, *Adv. Mater.* **2017**, 29, 1603774; b) Y. Lee, J. Suntivich, K. J. May, E. E. Perry, Y. Shao-Horn, *J. Phys. Chem. Lett.* **2012**, 3, 399.
- [30] a) B. Q. Li, C. Tang, H. F. Wang, X. L. Zhu, Q. Zhang, *Sci. Adv.* **2016**, 2, e1600495; b) B. Q. Li, S. Y. Zhang, C. Tang, X. Y. Cui, Q. Zhang, *Small* **2017**, 13, 1700610; c) G. L. Tian, M. Q. Zhao, D. S. Yu, X. Y. Kong, J. Q. Huang, Q. Zhang, F. Wei, *Small* **2014**, 10, 2251.
- [31] M. Jahan, Q. L. Bao, K. P. Loh, *J. Am. Chem. Soc.* **2012**, 134, 6707.
- [32] H. J. Tang, H. J. Yin, J. Y. Wang, N. L. Yang, D. Wang, Z. Y. Tang, *Angew. Chem., Int. Ed.* **2013**, 52, 5585.
- [33] C. Y. Lin, L. P. Zhang, Z. H. Zhao, Z. H. Xia, *Adv. Mater.* **2017**, 29, 1606635.
- [34] a) J. Y. Qu, S. Yan, X. H. Qu, S. J. Dong, *Electroanalysis* **2004**, 16, 1444; b) K. Flechtner, A. Kretschmann, H. P. Steinruck, J. M. Gottfried, *J. Am. Chem. Soc.* **2007**, 129, 12110.
- [35] a) P. Zhang, F. Sun, Z. H. Xiang, Z. G. Shen, J. Yun, D. P. Cao, *Energy Environ. Sci.* **2014**, 7, 442; b) H. W. Liang, W. Wei, Z. S. Wu, X. L. Feng, K. Mullen, *J. Am. Chem. Soc.* **2013**, 135, 16002.
- [36] a) M. A. U. Din, F. Saleem, B. Ni, Y. Yong, X. Wang, *Adv. Mater.* **2017**, 29, 1604994; b) D. Sebastian, A. Serov, K. Artyushkova, J. Gordon, P. Atanassov, A. S. Arico, V. Baglio, *ChemSusChem* **2016**, 9, 1986.
- [37] C. C. L. McCrory, S. H. Jung, J. C. Peters, T. F. Jaramillo, *J. Am. Chem. Soc.* **2013**, 135, 16977.
- [38] Y. Gorlin, T. F. Jaramillo, *J. Am. Chem. Soc.* **2010**, 132, 13612.
- [39] a) C. M. Chen, Q. Zhang, M. G. Yang, C. H. Huang, Y. G. Yang, M. Z. Wang, *Carbon* **2012**, 50, 3572; b) C. Y. Chen, C. Tang, H. F. Wang, C. M. Chen, X. Y. Zhang, X. Huang, Q. Zhang, *ChemSusChem* **2016**, 9, 1194.
- [40] a) G. Kresse, J. Furthmüller, *Phys. Rev. B* **1996**, 54, 11169; b) G. Kresse, J. Furthmüller, *Comput. Mater. Sci.* **1996**, 6, 15.
- [41] a) G. Kresse, D. Joubert, *Phys. Rev. B* **1999**, 59, 1758; b) P. E. Blöchl, *Phys. Rev. B* **1994**, 50, 17953.
- [42] J. P. Perdew, K. Burke, M. Ernzerhof, *Phys. Rev. Lett.* **1996**, 77, 3865.
- [43] S. Grimme, J. Antony, S. Ehrlich, H. Krieg, *J. Chem. Phys.* **2010**, 132, 154104.